



Boosting reactivity of water-gas shift reaction by synergistic function over $\text{CeO}_{2-x}/\text{CoO}_{1-x}/\text{Co}$ dual interfacial structures

Received: 19 March 2023

Accepted: 16 October 2023

Published online: 27 October 2023

Check for updates

Xin-Pu Fu^{1,4}, Cui-Ping Wu^{1,4}, Wei-Wei Wang¹, Zhao Jin¹, Jin-Cheng Liu²✉, Chao Ma³✉ & Chun-Jiang Jia¹✉

Dual-interfacial structure within catalysts is capable of mitigating the detrimentally competitive adsorption during the catalysis process, but its construction strategy and mechanism understanding remain vastly lacking. Here, a highly active dual-interfaces of $\text{CeO}_{2-x}/\text{CoO}_{1-x}/\text{Co}$ is constructed using the pronounced interfacial interaction from surrounding small CeO_{2-x} islets, which shows high activity in catalyzing the water-gas shift reaction. Kinetic evidence and in-situ characterization results revealed that CeO_{2-x} modulates the oxidized state of Co species and consequently generates the dual active $\text{CeO}_{2-x}/\text{CoO}_{1-x}/\text{Co}$ interface during the WGS reaction. A synergistic redox mechanism comprised of independent contribution from dual functional interfaces, including $\text{CeO}_{2-x}/\text{CoO}_{1-x}$ and $\text{CoO}_{1-x}/\text{Co}$, is authenticated by experimental and theoretical results, where the $\text{CeO}_{2-x}/\text{CoO}_{1-x}$ interface alleviates the CO poison effect, and the $\text{CoO}_{1-x}/\text{Co}$ interface promotes the H_2 formation. The results may provide guidance for fabricating dual-interfacial structures within catalysts and shed light on the mechanism over multi-component catalyst systems.

Previous findings have validated that the surface reaction normally proceeded at the metal-support interface upon the numerous hybrid catalysts^{1–4}. The most well-known strategy is anchoring metal atoms onto the surface of oxide support to establish mono-interfacial structure^{5–7}, while the ubiquitously competitive adsorption between reactant and product molecules would inevitably interfere with catalytic efficiency^{8,9}. From this perspective, a strategy based on the synergistic participation of dual interfaces is validated as an efficient path for catalyst design targeted for industrial catalysis processes^{3,10}. However, the efficiently targeted fabrication of the dual interface is impeded by the intricacy of the multifarious sorption ability desired for the catalysis process^{11–14}.

As a reducible transition metal, cobalt is promising for dual-interface design based on the prerequisite that dual kinds of Co species could integrate the advantages of each component^{14–16}. The

metallic Co^0 atom is commonly regarded as an active site for activating CO molecules in kinds of catalysis processes owing to its intense CO adsorption energy and electron-donor character¹⁷. The importance of Co^{2+} to the optimum adsorption/coverage of reactants or intermediates has been gradually recognized in recent studies^{14,15,18}. The co-presence of Co and CoO_x on the surface of Al_2O_3 or ZrO_2 was favorable for CO/ CO_2 activation and C-H bond scission^{19,20}. The structural engineering of Co-based catalysts aiming to establish highly active and stable dual-interface targeting to specific catalysis processes is thus desirable. However, fabricating a stable abundance Co/ CoO_x interface within an analogous Co/ CoO_x/MO_x structure is severely impeded by the unstable feature of $\text{Co}^{2+}(\text{CoO})$ species, especially under a reductive atmosphere^{11,12,21}. Meanwhile, the respective role of each interface and the corresponding synergistic mechanism have been insufficiently substantiated so far^{12–15,22}. A possible approach to overcoming the

¹Key Laboratory for Colloid and Interface Chemistry, Key Laboratory of Special Aggregated Materials, School of Chemistry and Chemical Engineering, Shandong University, 250100 Jinan, China. ²Center for Rare Earth and Inorganic Functional Materials, School of Materials Science and Engineering & National Institute for Advanced Materials, Nankai University, 300350 Tianjin, China. ³College of Materials Science and Engineering, Hunan University, 410082 Changsha, China. ⁴These authors contributed equally: Xin-Pu Fu, Cui-Ping Wu. ✉e-mail: liujincheng@nankai.edu.cn; cma@hnu.edu.cn; jjacj@sdu.edu.cn

above obstacles is modulating the oxidized state of metal atoms via modifying the metal-support interaction^{23,24}.

CeO₂ is encouraging for enhancing the stability of CoO_x species and establishing efficient dual interfacial Co-based catalysts because the defective structures (O_v(CeO₂)) derived from spontaneous Ce³⁺/Ce⁴⁺ change, which are prone to provide activated O species and thus more readily modulate the oxidized state of atoms at the interface²⁵. In this work, we reported the crucial role of CeO_{2-x} in maintaining the CoO phase under reductive conditions, resulting in the fabrication of a stable CeO_{2-x}/CoO_{1-x}/Co dual-interfaces structure. The as-formed CeO_{2-x}/CoO_{1-x}/Co structure efficiently catalyzes the water gas shift (WGS) reaction (CO + H₂O ⇌ CO₂ + H₂), a vital process for both model catalysis and hydrogen upgrading applications^{13,14,26–28}. The in situ characterization and DFT calculation disclosed that CeO_{2-x}/CoO_{1-x} and Co/CoO_{1-x} interfaces are synergistically involved in reaction cycles. The findings in this work provide a strategy to optimize the sorption process upon the catalyst surface via dual-interfacial engineering.

Result and discussion

Catalytic performance of CeCoO_x catalysts

The CeCoO_x catalysts were prepared through an ultrasonic spray approach (Supplementary Fig. 1) with tunable atomic ratios of Ce/Co for the raw materials (Ce/Co = 1/9, 9/1 and 0/10), labeled by 1Ce9CoO_x, 9Ce1CoO_x and Co₃O₄ respectively^{29,30}. The overall structure illustrated in transmission/scanning electron microscopy (TEM/SEM) images (Fig. 1a and Supplementary Fig. 2) revealed that the Co and Ce species were assembled into a spherical framework. As shown in Supplementary Fig. 3, apart from the weak diffracted peaks for the Co₃O₄ phase, non-detectable crystallized CeO₂ can be identified in the XRD patterns of the fresh 1Ce9CoO_x catalyst, suggesting the small crystallized size of CeO₂. The elemental mapping results (Supplementary Fig. 4) further illustrated the Co and Ce species homogeneously distributed over the

1Ce9CoO_x sample. In contrast with pristine Co₃O₄ catalyst, the averaged Co₃O₄ crystal size in the 1Ce9CoO_x determined by the Scherrer equation is much smaller (ca. 15.4 vs. 6.1 nm), indicating the influential role of the minor CeO₂ species in stabilizing and dispersing predominantly present Co species.

The as-prepared samples were evaluated as catalysts for the WGS reaction after pretreating by 5%H₂/Ar at 400 °C for 1 h. The CO conversions were valued with the WGS reaction temperatures elevated from 180 to 320 °C. In detail, the CO conversion of 1Ce9CoO_x reached 28% at ca. 240 °C with a high gas hourly space velocity (GHSV) of 168,000 mL g⁻¹ h⁻¹ (Supplementary Fig. 5), which was tremendously better than that of the Co₃O₄ catalyst (3%). This gap in CO conversion between the 9Ce1CoO_x and bare Co₃O₄ catalysts was further widened with a relatively low GHSV of 42,000 mL g⁻¹ h⁻¹ at ca. 240 °C (95% vs. 14% as illustrated in Fig. 1b). Otherwise, the pristine CeO₂ was almost inactive in catalyzing the WGS reaction as the reaction temperature below 300 °C, suggesting that the momentous synergetic effect present between CeO₂ and Co-related species. This hypothesis is further evidenced by the kinetic experiments. The apparent activation energy (*E*_a) value was distinctly decreased (Supplementary Fig. 6) for the 1Ce9CoO_x catalyst (100.7 kJ/mol) as compared with that of the Co₃O₄ catalyst (188.4 kJ/mol), implying that the reactant molecules might react through an advantageous reaction pathway upon the 1Ce9CoO_x catalyst.

The 1Ce9CoO_x catalyst demonstrated a remarkable mass-normalized reaction rate of 169.3 mmol_{CO}/g_{cat}/h at 250 °C (Fig. 1c, Supplementary Table 1), 3-folds of the value of 50.1 mmol_{CO}/g_{cat}/h for the 1Al9CoO_x catalyst with irreducible Al₂O₃ species, indicative of the exclusive role of reducible CeO₂ in activating Co species. The boosted activity of 1Ce9CoO_x catalyst was also higher than commercial CuZnAl catalyst and noble Au-Cluster/CeO₂ catalyst (64.8 and 27.8 mmol_{CO}/g_{cat}/h, Supplementary Table 1) under the same reaction condition^{31,32}. The 1Ce9CoO_x catalyst revealed good stability during the long-term

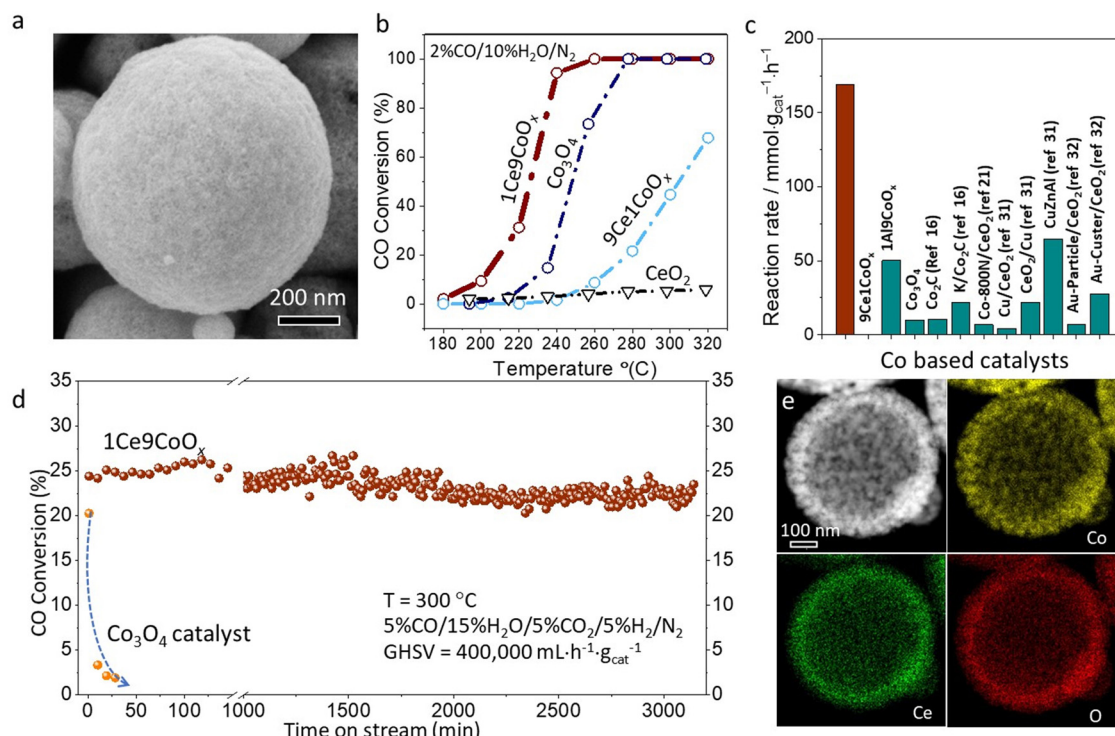


Fig. 1 | The catalytic performance and structural characterization of catalysts. **a** SEM image of fresh 1Ce9CoO_x catalyst. **b** CO conversions of WGS reaction over the 1Ce9CoO_x, Co₃O₄ and 9Ce1CoO_x catalysts at various temperatures. Reaction condition: 2%CO/10%H₂O/N₂, GHSV = 42,000 mL/g_{cat}/h. **c** Comparison of the reaction rate with reference catalysts at 250 °C^{16,21,31,32}. The detailed reaction

conditions and CO conversions for these catalysts are summarized in Supplementary Table 1. **d** Stability test results of the 1Ce9CoO_x and Co₃O₄ catalysts evaluated at 300 °C. Other reaction condition: 5%CO/15%H₂O/5%CO₂/5%N₂, GHSV = 400,000 mL g_{cat}⁻¹ h⁻¹. **e**, HAADF-STEM image and X-ray EDS elemental mappings (Co, Ce, and O) for the spent 1Ce9CoO_x catalyst.

test at 250 °C for 1800 min with a mild reaction atmosphere of (2%CO/10%H₂O/N₂), which outperformed the performance of the Co₃O₄ catalyst (Supplementary Fig. 7). To be noted, the gap in stability between 1Ce9CoO_x and Co₃O₄ catalyst was more significant under a relatively harsh reaction condition ($T = 300\text{ °C}$, 5%CO/15%H₂O/5%H₂/5%CO₂/N₂, GHSV = 400,000 mL g_{cat}⁻¹ h⁻¹), where the 1Ce9CoO_x was relatively stable over 3000 min on stream and the bare Co₃O₄ catalyst rapidly deactivated from 20% to 2% in the initial 40 min (Fig. 1d). The spent 1Ce9CoO_x catalysts were primarily explored by the aberration-corrected high-angle annular dark-field scanning transmission electron microscopy (ac-HAADF STEM). Supplementary Fig. 8 depicted that the nanoparticles within the spent 1Ce9CoO_x catalyst maintained assembled sphere morphology. Elemental mapping results proved that the Co and Ce species distributed homogeneously after either transient (Fig. 1e and Supplementary Fig. 9) or a long-term WGS reaction test (Supplementary Fig. 10). The average diameter of CeO₂ and CoO species derived from statistical results based on the HRTEM images were about 4.0 and 4.3 nm, where the lattice distance of all nanoparticles was verified prior to counting (Supplementary Figs. 11, 12). The aforementioned results evidenced the essential role of introduced CeO₂ species in enhancing the catalytic efficiency and stability during catalyzing WGS reaction for the CeCoO_x catalyst.

Identification of the CeO_{2-x}/CoO_{1-x}/Co dual-interface structure

The as-formed CeO_{2-x} nanoparticles with a ca. 2–4 nm diameter were located neighboring Co species (Fig. 2a–c, Supplementary Fig. 13), which were in line with the mean size as derived from HRTEM images or the XRD results based on the Scherrer Formula (CeO₂: -4.3 nm and CoO: -4.2 nm). In sharp comparison, the nanoparticles within the Co₃O₄ sample seriously aggregated after the long-term WGS reaction, as shown in Supplementary Fig. 14, suggesting that the presence of CeO₂ species effectively inhibits the excessive crystallization of Co species under the WGS reaction condition. In most cases, the optimal metal-oxides interface was commonly achieved by anchoring highly dispersed metal sites onto the surface of oxide support. In contrast, the inevitable growth of metal species, especially under reductive conditions, results in the irreversible loss of specific sites at the interface^{8,9}. The amount of the CeO₂-Co interfacial sites within the 1Ce9CoO_x catalyst was defined by the perimeter outline of small CeO_{2-x} particles with favored thermostability, which consequently resist the loss of interfacial Co-CeO₂ sites under reaction conditions.

The coexistence of metallic Co and CoO was also demonstrated by the XRD and XAFS results as shown in Supplementary Fig. 15 and Fig. 16. Lattice distances of 0.20, 0.24, and 0.27 nm respectively ascribed to Co(111), CoO(111) and CeO₂(200) were identified as shown in Fig. 2a, where the dominant CoO phase was identified in the region between metallic Co and CeO₂ (Fig. 2a, b) or directly anchored with CeO₂ nanoparticles (Supplementary Fig. 13). Similarly, as proven by the elemental mapping results, the differentiated distribution of Ce and Co implied that the CeO₂ islets interspersed among the Co species (Fig. 2c). The XPS spectra collected before and after light-off WGS reaction was collected and deconvoluted. As shown in Fig. 2d, the fresh 1Ce9CoO_x catalyst was characterized by the Co 2p_{3/2} binding energy at 779.9 eV and a shake-up satellite signal at 790.4 eV with low intensity, which is the typical feature for the Co²⁺/Co³⁺ ions in the Co₃O₄ spinel structure. The primary presence of the Co₃O₄ phase for the fresh 1Ce9CoO_x catalyst was also confirmed by the Raman results, as shown in Supplementary Fig. 3b. After the light-off WGS reaction (2%CO/10% H₂O/Ar), the binding energy of Co species was observed at 780.1 eV coupling with a strong satellite peak at 6.1 eV higher, which was typically ascribed to CoO phase³³. Only Co²⁺ ions in octahedral sites of rock-salt CoO may result in these typical photoemission features, where the Co²⁺ ions in Co₃O₄ do not locate on octahedral sites¹⁴. The spin-orbit coupling peak at ca. 16.0 eV higher was also a characteristic feature for CoO³³, which could be clearly identified for the spent

1Ce9CoO_x catalyst. In addition, a small shoulder peak at 778.0 eV ascribed to metallic Co was detected after the WGS reaction. Based on the above comparison, an unambiguous change from Co₃O₄ to Co/CoO upon the surface of the 1Ce9CoO_x catalyst was induced by the pretreatment and the WGS reaction. The Ce 3d spectrum was deconvoluted and labeled according to Burroughs formalism (Fig. 2e), where the fitted u' and u⁰ resulted from Ce³⁺. Interestingly, compared with fresh catalyst, the Ce³⁺ fraction was significantly boosted from 0.15 to 0.28, indicating that the amount of O_v-Ce increased after the WGS reaction. A similar conclusion could be derived from the O 1s results (Fig. 2f), in which the vacancy-related O species (O2 and O3) were increased from 0.40 to 0.68 after the WGS reaction³⁴. In addition, it should be noted that the relative amount of Ce³⁺ species upon the surface layer as determined by XPS results was lower than 0.03 (Ce³⁺/(CeO_x + CoO_x)), suggesting that the O species related with O_v-Ce³⁺ structure should be a minor component. Videlicet, this discrepancy indicated the plausible presence of CoO_{1-x} species upon the surface of the 1Ce9CoO_x catalyst.

To exclude the plausible interference from oxidation, quasi in situ XPS experiments were conducted over the 1Ce9CoO_x catalyst (2%CO/3% H₂O/Ar, 250 °C) to further estimate the reconstruction process of Co species during the WGS reaction. Supplementary Fig. 17a shows the Co 2p photoemission feature of 1Ce9CoO_x catalyst where the robust satellite peaks at ca. 786.2 eV indicate that the dominant presence of CoO on the surface layer of 1Ce9CoO_x was generated during the WGS reaction instead of being oxidized by the air. The Ce³⁺ content ($\mu^0 + \mu^1$) as a percentage of total cerium content was calculated to be 0.24 over 1Ce9CoO_x catalyst after in situ WGS reaction (Supplementary Fig. 17b), proving the abundant generation of O_v(CeO₂) under reaction condition³⁵. The corresponding CO conversions for various catalysts were determined with the comparable conditions (260 °C, 2%CO/3%H₂O/Ar), where the 1Ce9CoO_x catalyst demonstrated much better catalytic performance than the reference catalysts (Supplementary Fig. 18).

The presence of defective sites over the 1Ce9CoO_x and bare Co₃O₄ catalysts was further explored by the Raman experiments. The peaks at 191, 484, and 690 cm⁻¹ were detectable for fresh 1Ce9CoO_x catalyst (Supplementary Fig. 3), which were attributed to F_{2g}, E_g and A_{1g} symmetry modes of the crystalline Co₃O₄ respectively³⁶. After in situ feeding 2%CO/3%H₂O/Ar upon the surface of 1Ce9CoO_x catalyst at 250 °C, three peaks at regions of ca. 450, 530–550, and 580 cm⁻¹ were observed as shown in Fig. 2g, whereas they were absent for pristine Co₃O₄ catalyst (Supplementary Fig. 19). According to previous reports, the signals at ca. 450 and 580 cm⁻¹ could be ascribed to the F_{2g} mode and defect-induced mode (DI) of the ceria fluorite phase^{37–40}. There are two plausible affiliations for the signal at the region of 530–550 cm⁻¹: it might be derived from the oxygen vacancies within the surface or sub-surface layer of CeO₂ nanoparticles (surface O_v(CeO₂))³⁷; or the possible presence of oxygen vacancy in CoO phase (O_v(CoO)) contribute to this Raman signal³⁶. On the basis of the predominant presence of Co²⁺ in CoO identified by XPS results (Fig. 2d), we tend to attribute the Raman peak at the region of 530–550 cm⁻¹ to the combinative signals of O_v(CeO₂) and O_v(CoO) within the CeO_{2-x}/CoO_{1-x} interface region. As shown in Supplementary Fig. 20, the presence of the O_v(CoO) was also supported by the EELS results for the spent 1Ce9CoO_x catalyst. The calculated L₃/L₂ ratio for Co L-edge collected in the Co-rich region was ca. 3.2. In contrast, the corresponding values calculated for regions overlapped with CeO₂ increased to ca. 4.8. The intensity ratio of L₃/L₂ is determined by the occupation state of 3d-states, which the increased L₃/L₂ value might thus indicate the lower valence state of Co species induced by the creation of oxygen vacancies within the interface region³⁴. The facile formation of oxygen vacancies on CoO_{1-x} could result from a larger Co–O bond length and relatively weak bond strength in rock-salt CoO, in contrast to those of Co₃O₄¹⁴.

In addition, the presence of CeO_{2-x}/CoO_{1-x} and Co/CoO_{1-x} interface within the spent 1Ce9CoO_x catalysts was carefully substantiated by

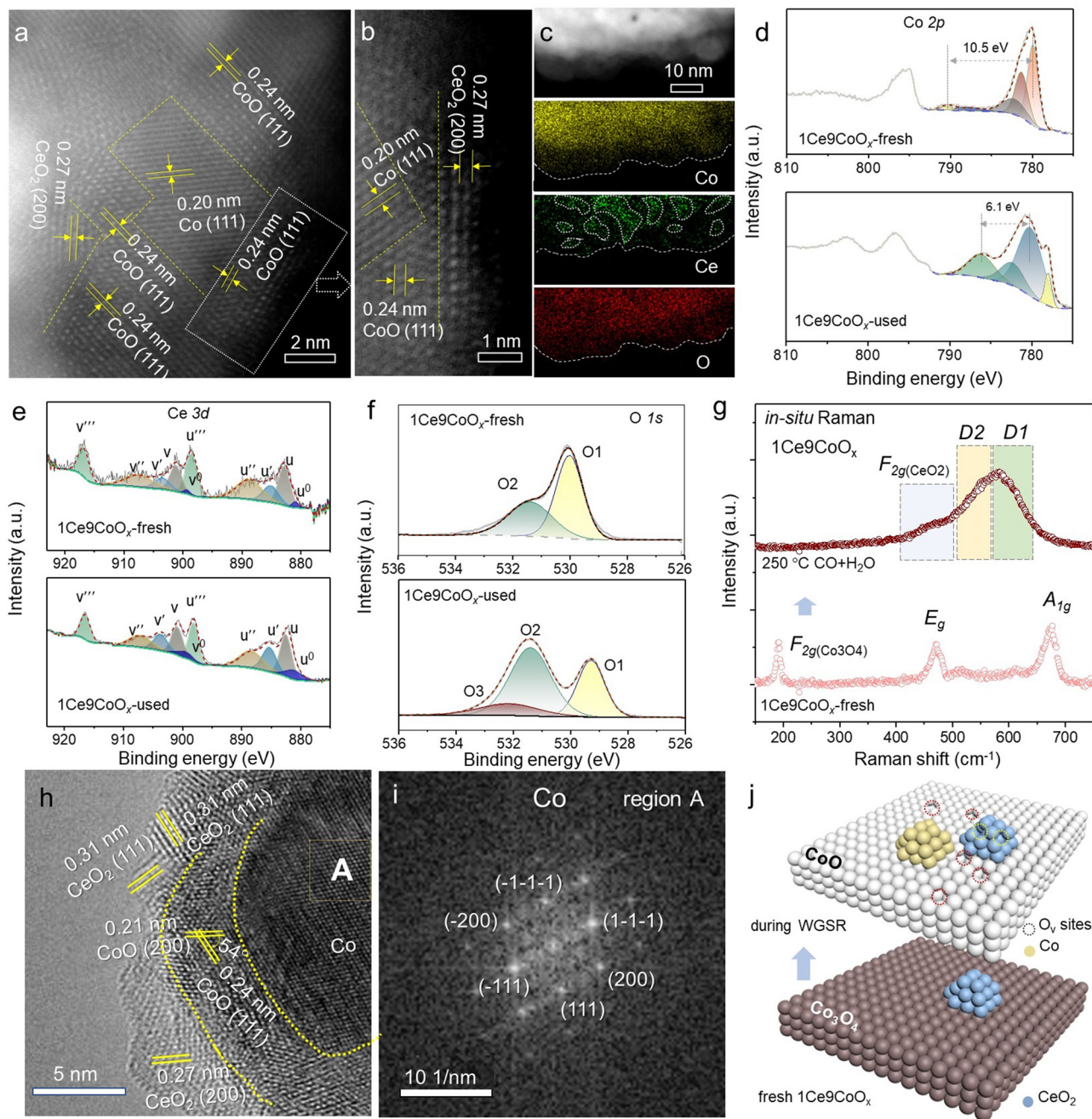


Fig. 2 | Identification of the reconstructed $\text{CeO}_{2-x}/\text{CoO}_{1-x}/\text{Co}$ dual-interfaces after WGS reaction. **a** HAADF-STEM images; **(b)** magnified STEM image; **(c)** elemental mappings (Co, Ce, and O) for the selected area of $1\text{Ce}_9\text{CoO}_x$ catalyst after light-off WGS reaction test. **d–f** XPS spectra of fresh and used $1\text{Ce}_9\text{CoO}_x$: **(d)** Co $2p$, **(e)** Ce $3d$ and **(f)** O $1s$ spectra. The XPS spectra for the spent catalyst were collected

after light-off WGS reaction ($2\%\text{CO}/10\%\text{H}_2\text{O}/\text{Ar}$, $180\text{--}320\text{ }^\circ\text{C}$). **g** in situ Raman spectra collected under WGS reaction condition at $250\text{ }^\circ\text{C}$. **h** HRTEM image of spent $1\text{Ce}_9\text{CoO}_x$ catalyst, where the interfacial region is illustrated by dotted line. **i** the corresponding FFT image of selected region A in Fig. 2h. **j** Schematic illustration of the phase transformation within the $1\text{Ce}_9\text{CoO}_x$ catalyst during the WGS reaction.

microscopy evidence. As shown in Fig. 2h, the crystal lattice spacing ascribed to $\text{CeO}_2(100)$, $\text{CoO}(111)$, and $\text{Co}(100)$ could be identified, where the boundary as marked by the dotted line was correspondingly contributed to $\text{CoO}_{1-x}/\text{Co}$ or $\text{CeO}_{2-x}/\text{CoO}_{1-x}$ interfaces. Specifically, the metallic Co species are generally found in the central zone, which is further proven by the corresponding FFT image as shown in Fig. 2i. More importantly, the coexistence of CoO and CeO_2 could always be identified in the same regions, such as the regions C as illustrated in Supplementary Figs. 21, 22, where it is adjacent to the metallic Co species in the central area. Similar results could be frequently observed in other HRTEM images, as shown in Supplementary Fig. 23, indicative

of the abundant presence of dual interfaces over the $1\text{Ce}_9\text{CoO}_x$ catalysts after the WGS reaction. Therefore, on the basis of the above microscopic and spectral evidence, we believed that the initial $\text{CeO}_2\text{-Co}_3\text{O}_4$ structure re-constructed to the $\text{CeO}_{2-x}/\text{CoO}_{1-x}/\text{Co}$ dual-interfaces during the WGS reaction (Fig. 2j).

Functions of $\text{CeO}_{2-x}/\text{CoO}_{1-x}$ and $\text{Co}/\text{CoO}_{1-x}$ dual-interfaces within the $1\text{Ce}_9\text{CoO}_x$ catalyst

As an indicator of the heterogeneous interaction, the oxygen reducibility of catalysts was determined by the H_2 temperature-programmed reduction ($\text{H}_2\text{-TPR}$) tests⁴¹. As shown in Fig. 3a, three peaks were

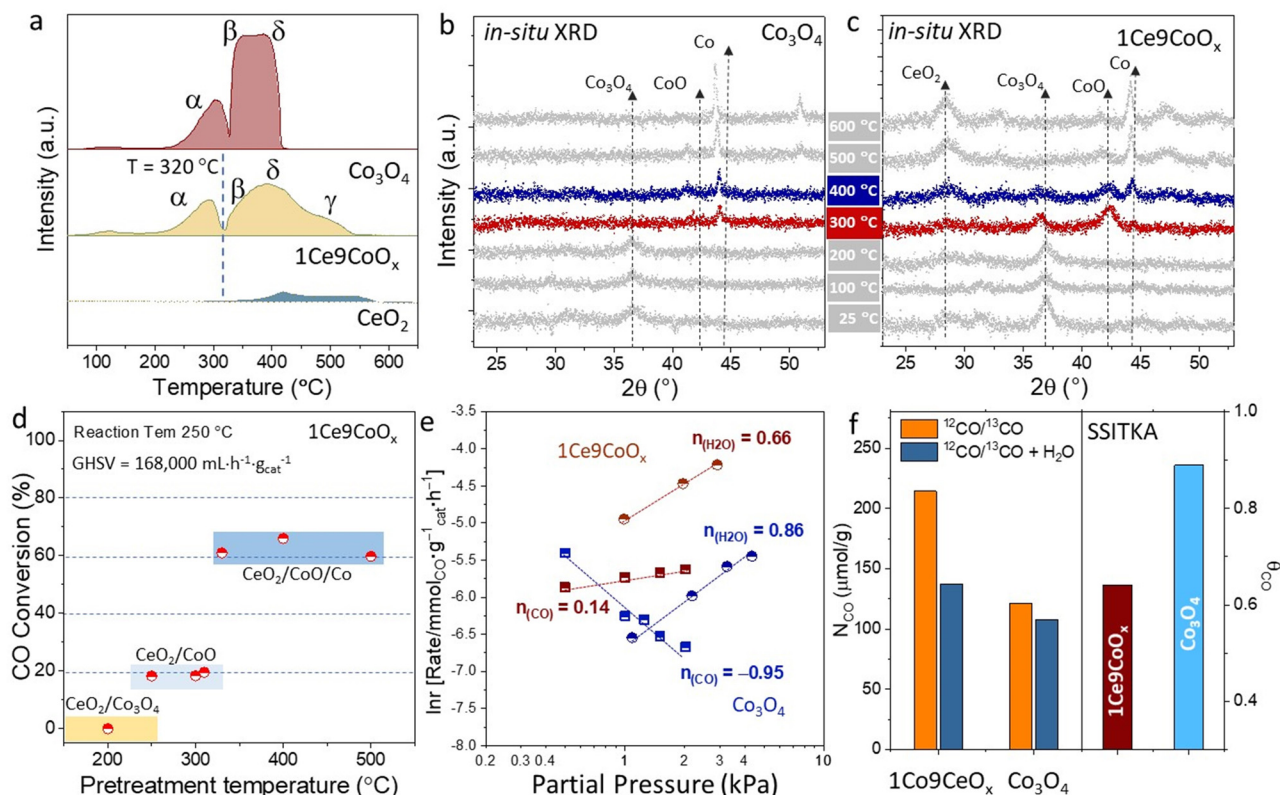


Fig. 3 | Investigation on the function of the dual interfaces. **a** H₂-TPR profile of 1Ce9CoO_x, Co₃O₄, and pristine CeO₂ samples. **b, c** The in situ XRD patterns were collected under 5% H₂/Ar atmosphere with different temperatures for the (b) Co₃O₄ and (c) 1Ce9CoO_x catalysts. **d** The CO conversions of WGS reaction at 250 °C for the

1Ce9CoO_x catalysts pretreated by 5% H₂/Ar under various temperatures. **e** Apparent reaction order of H₂O and CO for the 1Ce9CoO_x and Co₃O₄ catalysts. **f** The amount of adsorbed CO (N_{CO}) and the site coverage of CO (θ_{CO}) determined by the SSITKA results for the 1Ce9CoO_x and Co₃O₄ catalysts.

respectively identified for pristine Co₃O₄ at ca. 300, 350, and 410 °C, correspondingly denoted as the α , β and δ peak. In detail, the α reduction peak is indicative of the phase transformation from Co₃O₄ to CoO; the β and δ peaks imply the reduction process of surface or inner CoO to metallic Co, respectively^{15,42}. The ratio of peak area for $\alpha/(\beta+\delta)$ is 1/3.4, which is close to the stoichiometric ratio of 1/3. In comparison with the pristine Co₃O₄ catalyst, the 1Ce9CoO_x demonstrates a similar α reduction peak at around 290 °C, suggesting the comparable reduction behavior from Co₃O₄ to CoO for both catalysts. In addition, the relative intensity of β reduction peak was apparently decreased over 1Ce9CoO_x; meanwhile, one additional γ peak emerged at an elevated temperature of ca. 500 °C. To note, the $\alpha/(\beta+\delta+\gamma)$ value of 1/3.2 is close to the stoichiometric ratio of 1/3, implying that the γ peak might be derived from the reduction process of the CoO species strongly interacted with additive CeO₂. Videlicet, the surrounded CeO_{2-x} islets can play a vital role in maintaining the O-containing structure of Co species even at relatively high temperatures (>400 °C) under a reductive atmosphere. The ability of small CeO₂ nanoparticles to provide O atoms for oxidizing adjacent Co atoms was also validated by the auto-regenerated α peak as shown in the second-round TPR profile (Supplementary Fig. 24). These results demonstrated the pivotal role of CeO_{2-x} islets in fabricating the CeO_{2-x}/CoO_{1-x}/Co dual interface.

The in situ XRD patterns collected under the H₂ atmosphere were further used to substantiate the phase evolution over the 1Ce9CoO_x and Co₃O₄ catalysts. We observed a distinct phase transformation from Co₃O₄ to metallic Co over the pristine Co₃O₄ catalysts at 300 °C (Fig. 3b), coupling with negligible signal centered at 42.3° for the CoO phase. In sharp contrast, a remarkable diffracted peak at 42.3° for CoO emerged at 300 °C over the 1Ce9CoO_x sample, while the signal for

metallic Co is relatively weak at around 44.4°. This evidence is well consistent with the H₂-TPR results that the small CeO_{2-x} nanoparticles can maintain the oxidized state of Co species with a broader temperature range under reductive conditions, which is in line with its stabilization effect found in the previous report⁴³.

To validate the superiority of CeO_{2-x}/CoO_{1-x}/Co dual-interfaces, pretreatments with 5% H₂/Ar under various temperatures were conducted on the 1Ce9CoO_x to differentiate the initial phase state of catalysts (Fig. 3c and Supplementary Table 2), where the samples labeled by 1Ce9CoO_{x-x} respectively (x is pretreated temperatures). After pre-reducing at 200 °C (1Ce9CoO_{x-200}), the Co₃O₄ phase was predominant according to the in situ XRD results, and the 1Ce9CoO_{x-200} was almost inactive for catalyzing the WGS reaction. As the temperature elevated to 250 °C, the initial CO conversion was boosted to -20%, indicating that the CoO site is superior to Co₃O₄. Interestingly, compared with the 1Ce9CoO_{x-350} sample, the slightly lower reduction temperature of 320 °C led to a significant decrease in CO conversion from -60% to -20% for the 1Ce9CoO_{x-320}. This inflected temperature of 320 °C coincides nicely with the starting temperature of the β reduction process (Co²⁺ → Co⁰) as depicted in the H₂-TPR profile (Fig. 3a), indicating that metallic Co⁰ species is an essential component for the efficient catalysis process. Remarkably, physically mixed metallic Co catalysts and CeO₂ nanoparticles displayed an inferior CO conversion of 5.2% at 250 °C (Supplementary Table 1), proving that CoO sites induced by coordinated CeO_{2-x}/CoO_{1-x} interaction were also indispensable for highly active performance. Furthermore, the copresence of CoO and metallic Co coupling with best catalytic performance (Fig. 3d) was observed after in situ reduction under 5% H₂/Ar at 400 °C for the 1Ce9CoO_x, reconfirming the co-existing of dual active Co sites (Co⁰ and Co²⁺) was crucial for efficiently catalyzing WGS reaction.

The apparent reaction orders of H₂O and CO were determined at ca. 230 °C over the 1Ce9CoO_x and Co₃O₄ catalysts. The H₂O order on 1Ce9CoO_x is relatively lower than the Co₃O₄ catalyst (0.66 vs. 0.84, Fig. 3e), implying that the CeO_{2-x}/CoO_{1-x}/Co dual-interfaces have more substantial adsorption and coverage of O/OH/H₂O species than bare metallic Co surface. The CO order is 0.14 on the 1Ce9CoO_x catalyst, whereas the CO order for the Co₃O₄ catalyst is -0.95. The inverse-first order of CO upon bare Co⁰ sites within Co₃O₄ proved the excessively strong CO adsorption at relatively low temperatures^{17,23}, which might correspondingly block the active sites for the H₂O activation. The moderate CO adsorption ability for the 1Ce9CoO_x suggested that the CoO_{1-x}/Co interface behaved differently from its metallic counterpart²³. We further substantiate this speculation by conducting steady-state isotopic transient kinetic analysis (SSITKA) experiments over the 1Ce9CoO_x and Co₃O₄ catalysts. By in situ switching ¹²CO/He to ¹³CO/Ar with or without feeding 3%H₂O inside, the total number of active sites (N_{tot}) and adsorbed amount of reversibly adsorbed CO (N_{CO}) molecules under steady state were determined as shown in Supplementary Fig. 25⁴⁴. Subsequently, dividing the N_{CO} with N_{tot} gave the surface coverage of CO (θ_{CO}) with the presence of H₂O molecules. As shown in Fig. 3f, the metallic Co⁰ sites within the Co₃O₄ catalyst demonstrated a higher θ_{CO} of 0.89 in comparison with 0.64 for the

CoO_{1-x}/Co interface within 1Ce9CoO_x catalyst at 250 °C, further proving that the excessively stable CO molecules exactly impaired H₂O activation upon the pristine surface of metallic Co⁰. Therefore, the reconstructed CoO_{1-x}/Co interface effectively weakened the CO poisoning effect at the relatively low reaction temperature, which provides more active sites for the following surface reaction.

Synergistic reaction pathway proceeded upon CeO_{2-x}/CoO_{1-x} and CoO_{1-x}/Co dual-interfaces

In situ Raman spectra were sequentially collected under different modes over the 1Ce9CoO_x catalyst to offer a deeper insight into the detailed reaction pathway. Figure 4a depicted that numerous V_(CoO) and V_(CeO₂) with defect modes at ca. 540 and 580 cm⁻¹ were generated in the interface region over 1Ce9CoO_x catalyst when pretreating the 1Ce9CoO_x catalyst with 5%H₂/Ar at 400 °C. Based on previous reports, the value of the D/F_{2g} ratio can qualitatively represent the concentration of O_{v(CeO₂)}³⁷. Notably, the D_{(CeO₂)/F_{2g} ratio of -2.3 over 1Ce9CoO_x catalyst is much higher than that of the pristine CeO₂ nanoparticles with an averaged diameter of ca. 5–8 nm (D/F_{2g} = -0.1, Supplementary Fig. 26), indicative of the vastly boosted concentration of oxygen vacancy by forming CeO_{2-x}/CoO_{1-x} interface. When co-feeding CO and H₂O inside, the relative intensity of D mode signal at 540 cm⁻¹}

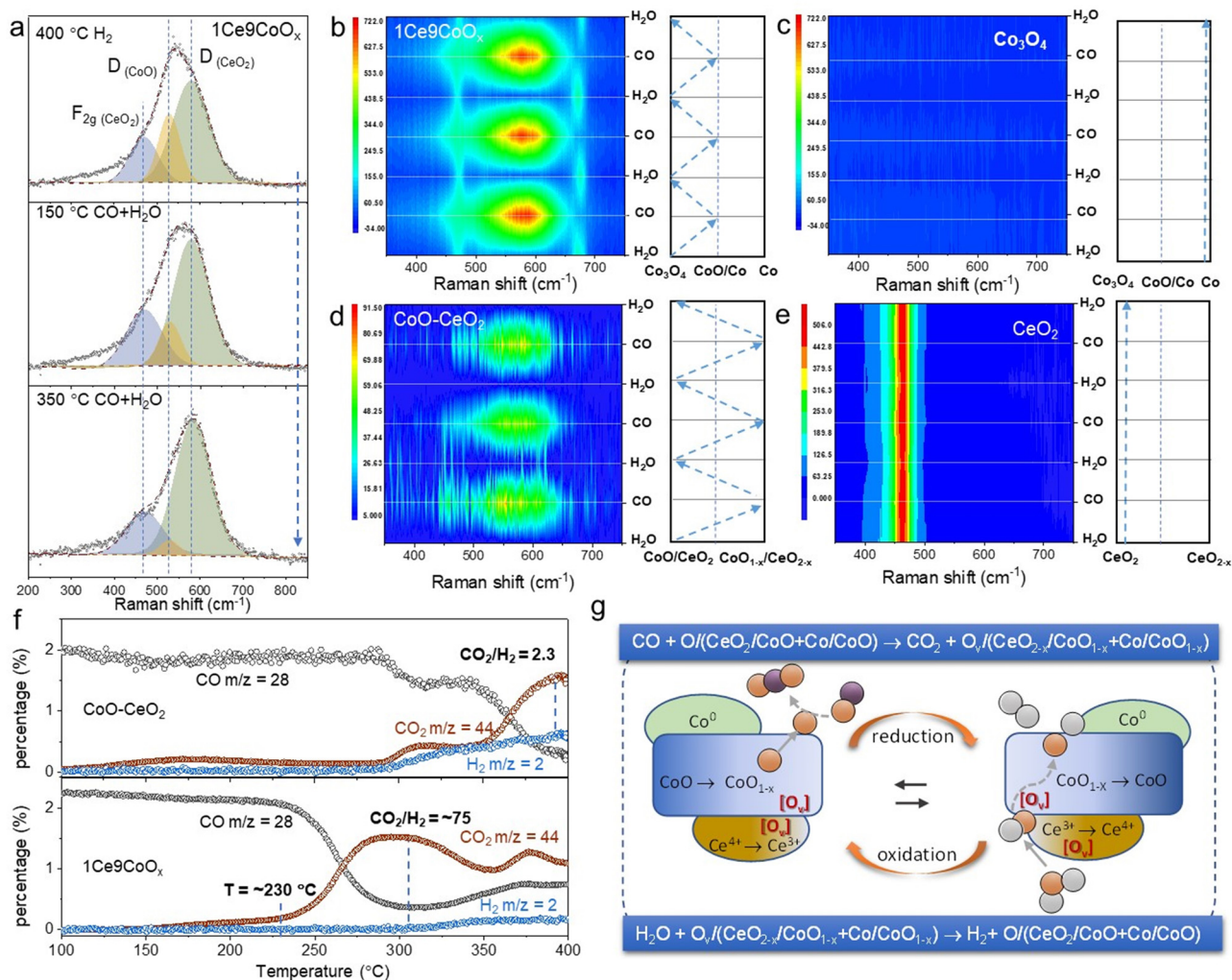


Fig. 4 | Study of the synergistic mechanism on the dual-interfaces. **a** In situ Raman spectra collected under 5%H₂/Ar or 2%CO/3%H₂O/Ar atmospheres at 400 °C. **b–e** In situ Raman spectra continuously collected as the feeding gas switched between 3%H₂O/Ar and 5%CO/Ar at 250 °C for **(b)** 1Ce9CoO_x, **(c)** Co₃O₄, **(d)** CoO-CeO₂ and **(e)** CeO₂ catalysts. The right part demonstrates the transformations

of Co and CeO₂ species during experiments. **f** CO-TPSR profile for the CoO-CeO₂ catalyst and 1Ce9CoO_x catalyst. The catalysts were pre-hydroxylated (3%H₂O/Ar, 250 °C) before experiments. **g** Schematic illustration of plausible WGS reaction pathway upon the CeO_{2-x}/CoO_{1-x}/Co dual interface.

apparently decreased at 150 °C and further weakened at 350 °C (Fig. 4a), suggesting that these vacancy structures participated in dissociating H₂O molecules and can be refilled by the dissociated O(H) species at elevated temperatures.

Next, the CO-H₂O switch test was used to visualize the stepwise process between the CeO_{2-x}/CoO_{1-x} and CoO_{1-x}/Co interfaces for the 1Ce9CoO_x catalyst (Fig. 4b). After feeding 3% H₂O/Ar onto the surface of 1Ce9CoO_x catalyst at 250 °C, typical E_g mode at 480 cm⁻¹ and A_{1g} mode at 680 cm⁻¹ for crystallized Co₃O₄ were observed, while the Raman signals at 540 and 580 cm⁻¹ for $V_{(\text{CoO})}$ and $V_{(\text{CeO}_2)}$ vanished. This experimental fact evidenced that the dissociated O(H) species from H₂O molecules can refill the vacant structures and oxidize the CeO_{2-x}/CoO_{1-x} interface at a relatively low temperature. Subsequently, the D mode signals at 540 and 580 cm⁻¹ for the $V_{(\text{CoO})}$ and $V_{(\text{CeO}_2)}$ recurred when feeding 5% CO/Ar inside, implying the reversible regeneration of vacancies and consumption of active O(H) species at the CeO_{2-x}/CoO_{1-x} interface. In sharp contrast, no detectable structure transformations were observed upon the pristine surface of metallic Co species during the continuous CO-H₂O switching tests for the Co₃O₄ catalyst (Fig. 4c), implying that the presence of CeO₂ is essential for boosting the H₂O activation ability.

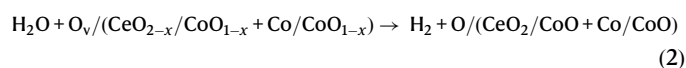
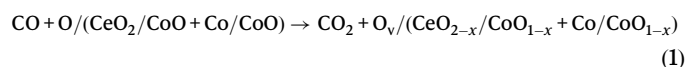
The CoO-CeO₂ catalyst and bare CeO₂ nanoparticles were prepared (Supplementary Figs. 27–29) and investigated further to dig out the role of the CoO/CeO₂ interface. Typical Raman active signals for CeO₂ centered at 463 cm⁻¹ (F_{2g} mode) and ca. 580 cm⁻¹ (D mode) could be identified during the CO-H₂O sequential switching tests (Fig. 4d). In the presence of CO molecules at 250 °C, the signal of D mode could be enhanced over the CoO-CeO₂ catalyst, implying that the O species occupied vacancies could be easily removed in this step. More importantly, this consumption of O species upon the vacancies could be regenerated as H₂O molecules purge inside. However, the bare CeO₂ demonstrated negligible variation for the D mode at 580 cm⁻¹ as CO or H₂O feeding inside (Fig. 4e), proving the low O species activity in the absence of the CoO/CeO₂ interface. This recyclability of O vacancies for the CoO-CeO₂ catalyst induced by gas switching between reactant molecules was indicative that the structural changes of CoO/CeO₂-CoO_{1-x}/CeO_{2-x} might participate in the CO oxidation step and H₂O dissociation step.

Additionally, it should be noted that the reversible structural changes over the CoO-CeO₂ catalyst were different from those of the 1Ce9CoO_x catalyst. As shown in Fig. 4b, typical phonon vibration signals at 480 cm⁻¹ (E_g mode) and 680 cm⁻¹ (A_{1g} mode) for Co₃O₄ were observed as the H₂O molecules fed inside, while it was absent for the CoO-CeO₂ catalyst (Fig. 4c). This implied that the oxidation behavior of the Co species should be strongly correlated with the presence of the Co/CoO interface over the 1Ce9CoO_x catalyst. Videlicet, the H₂O molecules could dissociate on the CoO/CeO₂ interface, while the dissociated O-related species were unable further to oxidize cobalt species without the Co/CoO interface. In addition, we collected the H₂-TPR profile for the 1Ce9CoO_x catalysts after the in situ WGS reaction (250C, 2%CO/3%H₂O/Ar). Interestingly, as shown in supplementary Fig. 30, another sharp peak centered at 172 °C was observed when the 1Ce9CoO_x was exposed to the feed gas, which might belong to the reduction of active O species generated by redox reaction cycles on the surface. As expected, this deduction was also supported by the CO-TPSR results. In the typical carboxyl pathway, the adsorbed CO molecules would react with the dissociated OH* group by forming the HOCO intermediate upon the surface of catalysts^{31,45}. Based on the prerequisite that adsorbed molecules reacted on the surface of the catalyst as CO + OH → CO₂ + 1/2H₂²⁶, the CO temperature-programmed surface reaction (CO-TPSR) test normally can validate such an association process from the stoichiometric ratio (1/2) for produced H₂ and CO₂. As shown in Fig. 4f, the generated products for the CoO-CeO₂ catalyst follow a CO₂/H₂ ratio of -2/1, implying that the O-related species involved in the surface reaction should be hydroxy groups

rather than active O atoms. However, when the Co/CoO interface was generated by pretreatment at 400 °C (Fig. 3c), the 1Ce9CoO_x catalyst with dual-interface structure demonstrated a distinctly different CO₂/H₂ evolution during the CO-TPSR test. Negligible H₂ (CO₂/H₂ » 2) was identified in the CO-TPSR profile over the hydroxylated 1Ce9CoO_x catalyst, indicating that the CO molecules on CoO_{1-x}/Co interface might be oxidized by activated O atoms rather than OH groups upon the dual-interfaces. Moreover, the evolution slope of produced CO₂ in CO-TPSR ($m/z = 44$, Fig. 4f) was well in step with the evolution of CO conversions as shown in Fig. 1b, in which the reaction activity increased sharply at about 230 °C. Such a correlation rationalized that the surface reaction between activated O atoms and CO molecules contributes primarily to the WGS reaction activity over the 1Ce9CoO_x catalyst. Based on these results, it is reasonable to conclude that the Co/CoO interface within the 1Ce9CoO_x catalyst was indispensable for dissociating H₂O molecules to active O atoms.

The H/D kinetic isotopic effect (KIE) has been widely used to explore the WGS reaction mechanism⁴⁶, owing to differentiated zero-point energies of the D- and H- labeled molecular species induced by the significant mass distinction between the D and H atoms. The relatively larger H/D KIE value of 5.6 indicated the O-D bond cleavage involved in the primary kinetic mode on the bare Co⁰ surface (Supplementary Fig. 31), implying that the breaking O-H in H₂O molecules should be the rate-determining step (RDS) of WGS reaction process over the surface of the pristine Co. In contrast, the 1Ce9CoO_x catalyst demonstrated a lower KIE value of 1.9, implying a normal isotopic effect on the CeO_{2-x}/CoO_{1-x} dual interface structure. Considering its H₂ reaction order of -0.9 (Supplementary Fig. 32), we speculated that a slow H transfer/spillover step might be involved in the reaction pathway 1Ce9CoO_x catalyst according to previous research findings⁴⁶.

Based on these observations mentioned above, as schematically illustrated in Fig. 4g, we propose that two sequentially redox steps were synergistically involved over the CeO_{2-x}/CoO_{1-x}/Co dual-interfaces while catalyzing the WGS reaction:



To verify the rationality of the proposed mechanism, we conducted DFT calculations to investigate the reaction path on the dual-interface structures. Since the above experimental data provided a strong indication that CoO sites modified the CO adsorption and CeO_{2-x} islets contribute to efficient H₂O activation, the reaction energy of elementary steps over Co⁰ sites or CeO_{2-x}/CoO interfacial sites was investigated. On the basis of the experimental characterization findings, we conducted three catalyst models as illustrated in Supplementary Fig. 33 (Co(0001), CeO_{2-x}/CoO(100) and Co₁₀/CoO(100)). The CO adsorption energy was determined to be -1.69 eV on the pristine Co(0001), which would thermodynamically compete for the H₂O dissociation process on the same Co⁰ sites (Supplementary Fig. 34). The intense CO adsorption on Co(0001) surface led to the poisoning of active sites and induced sequential high activation energy of 1.15 eV and 1.08 eV for forming *COOH intermediate and subsequently generating *CO₂ and *H₂ on Co(0001) surface, implying the detrimental effect of strong CO adsorption on independent Co⁰ sites. In contrast, the CeO_{2-x}/CoO interface showed moderate energy of -0.28 eV via the CO adsorption process upon Co²⁺ sites, and coupling with a reasonably low reaction barrier of 0.89 eV (TS1) to subsequently react with lattice O atom of CeO_{2-x} (Fig. 5a, b), resulting in the generation of an O_{v(CeO2-x)}

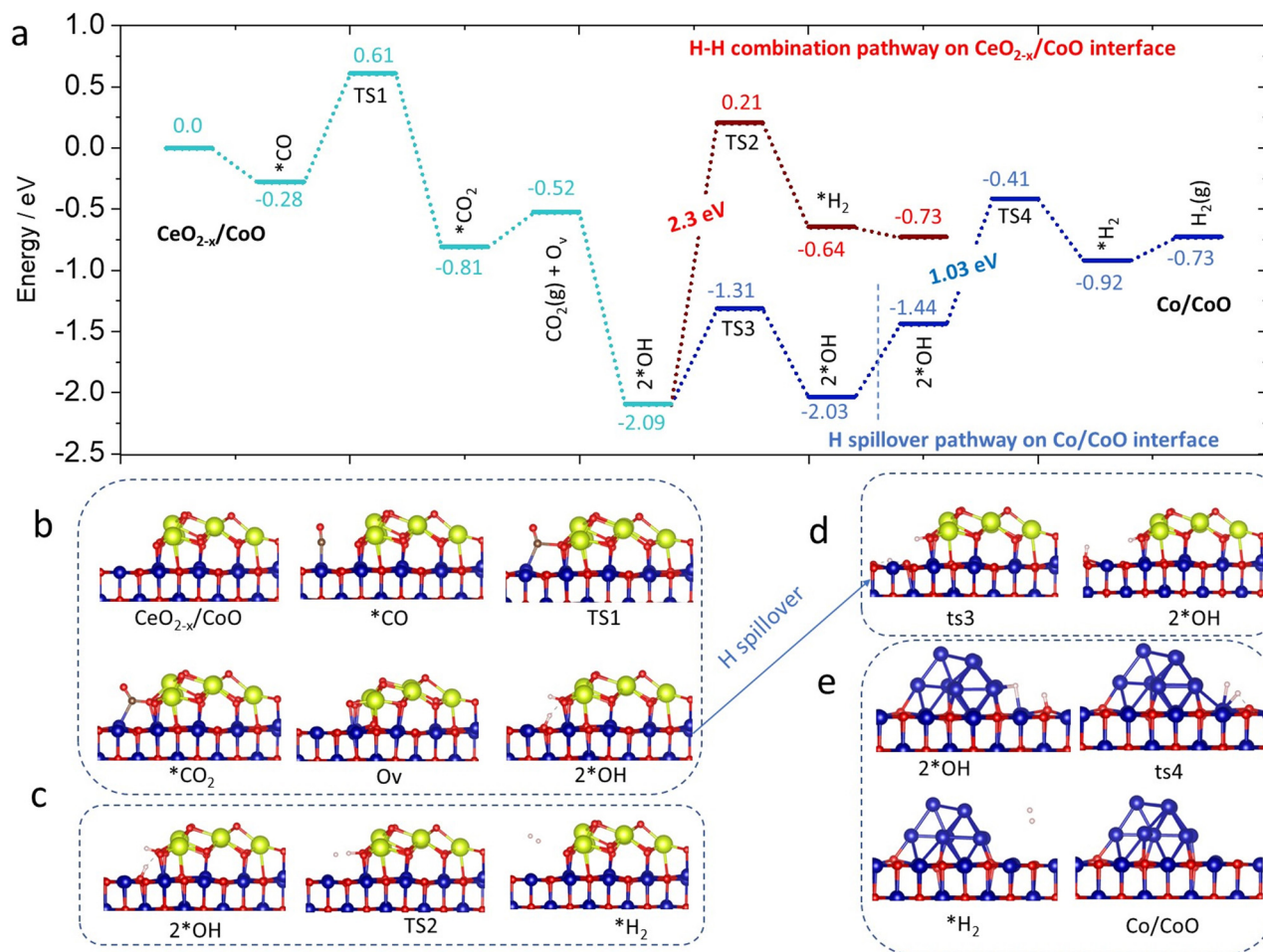


Fig. 5 | Reaction pathway and corresponding optimized structures for the water gas shift reaction over dual interfaces. **a** Energy profile for the CO oxidation with lattice O, H₂O dissociation and H₂ formation steps on the CeO_{2-x}/CoO(100) and Co₁₀/CoO(100) interfaces, respectively. The x-axis shows the reaction intermediates and transition states (TS); the y-axis demonstrates the relative

energy. **b** Structures of the CO molecules react with interfacial O from CeO_{2-x}. **c** Structures of the *H₂ derived through an H-H direct combination way on the CeO_{2-x}/CoO interface. **d** Illustrations of H diffusion on CoO(100) surface. **e** Illustrations of H₂ formation at the Co₁₀/CoO(100) interface. Co, Ce, O, and H atoms are shown in purple, yellow, red and white, respectively.

vacancy. As-formed O_v(CeO_{2-x}) within the CeO_{2-x}/CoO interface enables H₂O molecules to dissociate into two *OH with a favorable exothermic step of 1.28 eV, which is consistent with the superior activation ability of 1Ce9CoO_x catalyst as experimentally evidenced above.

To note, the metallic Co⁰ atoms are also prerequisite sites for high WGS activity according to experimental results shown in Fig. 3, whereas its exact function is still ambiguous in previous reports^{15,18,47}. In addition, our DFT calculation results demonstrated that the downstream step of H₂ direct formation from two independent *OH groups at CeO_{2-x}/CoO interface underwent the transition state of TS2 (Fig. 5c), which had an extremely high barrier of 2.3 eV (red line). A similar process was also found in calculation results for the Ir₇O_x/FeO_x catalyst that direct formation of *H₂ molecules from two independent H atoms revealed a disadvantageous energy barrier of 3.25 eV⁵. The enormous energy barrier implied that the single CeO_{2-x}/CoO interface is insufficient for a thermodynamically favored WGS reaction cycle. Comprehensively, in consideration of the indispensable role of metallic Co⁰ sites for an efficient catalysis process, we calculated the H₂ formation step at the Co₁₀/CoO(100) interface. As expected, the H atom diffuses on CoO(100) with a mild migration barrier of 0.78 eV (Fig. 5d). In addition, it is interesting that breaking the H atom from OH onto CoO(100) with the aid of the metal Co⁰ site is relatively facile with a rational energy barrier of 1.03 eV (Fig. 5e). The transition structure

(TS4) comprises H^{δ+} and H^{δ-} atoms that are coordinated with the O atom and Co⁰ atom, respectively (Supplementary Fig. 35). After two H atoms approach each other, the H₂ molecule is formed and only has physical adsorption at the Co⁰/CoO(100) interface, which could easily be removed. We underlined the synergistic participation of dual interfaces, CeO_{2-x}/CoO and Co⁰/CoO, in the proposed redox mechanism, which well rationalized our experimental finding as discussed above.

In summary, a highly active dual-interfacial catalyst was fabricated through a spray pyrolysis approach, demonstrating boosted WGS reaction activity than other Co-based catalysts and even comparable with some noble catalysts. We have conducted a combined experimental and theoretical study to explore the anthemically active structure and reaction pathway over the dual-interfacial structure. The CeO_{2-x}/CoO_{1-x}/Co dual-interfaces are structurally active for efficiently catalyzing WGS reaction, where the surrounded presence of small CeO_{2-x} islets is the induction for dominantly existing CoO_{1-x} in the intermediate region. The as-formed CoO_{1-x} can optimize the CO activation step by avoiding CO poisoning due to the excessively strong CO-Co⁰ binding. A redox mechanism comprising dual interfaces (CeO_{2-x}/CoO_{1-x} and Co/CoO_{1-x}) synergistically participating in a reaction cycle has been identified. The CeO_{2-x}/CoO_{1-x} interface offers an activated O atom to react with adsorbed CO molecule and also takes part in initially dissociating H₂O into two adsorbed OH groups. Directly breaking two

dissociated OH groups to form an H₂ molecule is energetically unfavorable at the CeO_{2-x}/CoO_{1-x} interface, while the H atoms are much easier to migrate and desorb at the Co/CoO_{1-x} interface.

Methods

Catalyst preparations

The CeCoO_x mesoporous hollow spheres were synthesized by a spray pyrolysis method⁴⁸. 8 mmol of mixed cobalt nitrate and cerium nitrate (molar ratio of Ce/Co is 1/9, 9/1, and 0/10) were added to the 60 mL ethanol. After 10 min stirring, the stock solution was transferred to the household ultrasonic humidifier to produce microspheres via the aerosol-spraying process. The atomized spray was sequentially carried by pure N₂ flow through a 90 cm -length glass tube placed in a tube furnace at 400 °C. Then, the hybrid powders were collected and further dried in an oven at 70 °C overnight. The reference catalyst of Al₁₉CoO_x was prepared with the same procedures described above, in which the molar ratio of Al/Co is 1/9.

Hydrogen temperature programmed reduction (H₂-TPR)

The H₂-TPR tests were conducted in a Builder PCSA-1000 instrument (Beijing, China) equipped with a thermal conductivity detector (TCD) to detect H₂ consumption. The fresh catalysts (ca. 30 mg, 20–40 mesh) were pretreated at 300 °C in the air (0.5 h). Following cooling to room temperature, the sample was flushed using pure N₂ at room temperature for about 30 min, then switched to 10% H₂/Ar and heated from room temperature to 900 °C with a ramping rate of 5 °C·min⁻¹. The second-round H₂-TPR profile for the catalyst was continuously collected after conducting the first-round test without exposure to air.

X-ray diffraction (XRD)

The ex-situ XRD patterns were obtained by a PANalytical X'pert3 powder diffractometer (40 kV, 40 mA, λ_{Cu-Kα} = 0.15418 nm) with an acquisition time of 8.5 min in the range of 10–90°. The in situ XRD patterns were obtained from the same machine with an Anton Paar XRK-900 reaction chamber. Samples were loaded in a ceramic sample holder (diameter of 10 mm; depth of 1 mm) and then treated with various conditions. The in situ reaction chamber was heated from room temperature to 600 °C (interval: 100 °C) with a ramping rate of 30 °C/min under 5% H₂/Ar (30 mL/min). Two rounds of measurements lasting for 20 min were carried out for each selected temperature. The second measurement round was collected and used to determine the structure of the catalysts.

Raman test

The ex-situ and in situ Raman spectra were recorded on a LabRAM HR800 spectrometer (HORIBA Jobin Yvon) using 473 nm laser excitation. The spectral resolution was 2 cm⁻¹ with a scanning range of 200 to 800 cm⁻¹. The micro-Raman in situ reactor (Xiamen TOPS) with a thermo-module was used for in situ experiments. Before each measurement, ca. 25 mg of the catalysts were pretreated in 5% H₂/Ar (99.997%, 30 mL/min) at 400 °C for 60 min. Then, the in situ Raman spectra were collected in the following two condition modes: (1) -3% H₂O/Ar or 5% CO/Ar with a flow rate of 30 mL/min alternatively flowed inside the reaction chamber at 250 °C; (2) the WGS reaction gas (5% CO/ ~3% H₂O/Ar, 30 mL/min) was continuously injected to the reaction cell at various temperatures. The six-way valve was used to avoid the plausible oxidation of the catalysts.

X-ray photoelectron spectroscopy (XPS)

X-ray photoelectron spectroscopy (XPS) analysis was carried out on an Axis Ultra X-ray photoelectron spectrometer using Al Kα radiations with the C 1s line at 284.8 eV calibrating the binding energies. Quasi in situ XPS experiments were conducted on a Thermo Scientific ESCALAB Xi+ XPS instrument.

Catalytic tests

A fixed-bed flow reactor was used for the WGS reaction tests on the catalysts. The reaction gas was 2% CO/10% H₂O/N₂ (99.997% purity), and the total GHSV was 42,000 or 168,000 mL g_{cat}⁻¹ h⁻¹. The catalyst was pretreated in synthetic air at 300 °C for 30 min before the measurement. The reactivity results of catalysts were measured from 150 to 300 °C per step under reaction gas. A non-dispersive IR spectroscopy was used to quantify the outlet gases online. The residual water was gathered in an ice trap before the IR gas analyzer.

Data availability

The main data supporting the findings of this study are available within the paper and its Supplementary Information. Additional data are available from the corresponding authors upon reasonable request. Source data are provided with this paper.

References

- Rodriguez, J. A. et al. Activity of CeO_x and TiO_x nanoparticles grown on Au(111) in the water-gas shift reaction. *Science* **318**, 1757–1760 (2007).
- Xu, K. et al. Catalytically efficient Ni-NiO_x-Y₂O₃ interface for medium temperature water-gas shift reaction. *Nat. Commun.* **13**, 2443 (2022).
- Xie, C., Niu, Z., Kim, D., Li, M. & Yang, P. Surface and interface control in nanoparticle catalysis. *Chem. Rev.* **120**, 1184–1249 (2020).
- Saavedra, J., Doan, H. A., Pursell, C. J., Grabow, L. C. & Chandler, B. D. The critical role of water at the gold-titania interface in catalytic CO oxidation. *Science* **345**, 1599–1602 (2014).
- Liang, J. X. et al. Dual metal active sites in an Ir1/FeO_x single-atom catalyst: a redox mechanism for the water-gas shift reaction. *Angew. Chem. Int. Ed.* **59**, 12868–12875 (2020).
- Guo, Y. et al. Low-temperature CO₂ methanation over CeO₂-supported Ru single atoms, nanoclusters, and nanoparticles competitively tuned by strong metal-support interactions and H-spillover effect. *ACS Catal.* **8**, 6203–6215 (2018).
- Yao, S. et al. Atomic-layered Au clusters on α-MoC as catalysts for the low-temperature water-gas shift reaction. *Science* **357**, 389–393 (2017).
- Campbell, C. T., Parker, S. C. & Starr, D. E. The effect of size-dependent nanoparticle energetics on catalyst sintering. *Science* **298**, 811–814 (2002).
- Simonsen, S. B. et al. Direct observations of oxygen-induced platinum nanoparticle ripening studied by in situ TEM. *J. Am. Chem. Soc.* **132**, 7968–7975 (2010).
- Bruix, A. et al. A New type of strong metal-support interaction and the production of H₂ through the transformation of water on Pt/CeO₂(111) and Pt/CeO_x/TiO₂(110) Catalysts. *J. Am. Chem. Soc.* **134**, 8968–8974 (2012).
- Lee, Y.-L. et al. Optimization of cobalt loading in Co-CeO₂ catalyst for the high temperature water-gas shift reaction. *Top. Catal.* **60**, 721–726 (2017).
- Vovchok, D. et al. In situ characterization of mesoporous Co/CeO₂ Catalysts for the high-temperature water-gas shift. *J. Phys. Chem. C* **122**, 8998–9008 (2018).
- Nagai, M. & Matsuda, K. Low-temperature water-gas shift reaction over cobalt-molybdenum carbide catalyst. *J. Catal.* **238**, 489–496 (2006).
- Zhang, S. et al. WGS catalysis and in situ studies of CoO_(1-x), PtCo_(n)/Co₃O₄, and Pt_(m)Co_(m)/CoO_(1-x) nanorod catalysts. *J. Am. Chem. Soc.* **135**, 8283–8293 (2013).
- Cao, Y. et al. Structural evolution of active entities on Co₃O₄/CeO₂ catalyst during water gas shift reaction. *Ind. Eng. Chem. Res.* **58**, 17692–17698 (2019).
- Sun, X.-C. et al. Weakening the metal-support interactions of M/CeO₂ (M = Co, Fe, Ni) using a NH₃-treated CeO₂ Support for an

- enhanced water–gas shift reaction. *ACS Catal.* **12**, 11942–11954 (2022).
- Li, M.-R. & Wang, G.-C. The mechanism of ethanol steam reforming on the Co⁰ and Co²⁺ sites: A DFT study. *J. Catal.* **365**, 391–404 (2018).
 - Zhan, Y. et al. Molecular-level understanding of reaction path optimization as a function of shape concerning the metal–support interaction effect of Co/CeO₂ on water–gas shift catalysis. *Catal. Sci. Tech.* **9**, 4928–4937 (2019).
 - Li, X. et al. Insights into the role of dual-interfacial sites in Cu/ZrO₂ catalysts in 5-HMF hydrogenolysis with isopropanol. *ACS Appl. Mater. Interfaces* **13**, 22292–22303 (2021).
 - Wang, L. et al. Selective hydrogenation of CO₂ to ethanol over cobalt catalysts. *Angew. Chem. Int. Ed.* **57**, 6104–6108 (2018).
 - Gnanamani, M. K. et al. Low temperature water–gas shift reaction over alkali metal promoted cobalt carbide catalysts. *Top. Catal.* **57**, 612–618 (2013).
 - Ge, Y. et al. Maximizing the synergistic effect of conical catalyst on alpha-MoC for robust hydrogen production. *J. Am. Chem. Soc.* **143**, 628–633 (2021).
 - Have, I. C. T. et al. Uncovering the reaction mechanism behind CoO as active phase for CO₂ hydrogenation. *Nat. Commun.* **13**, 324 (2022).
 - Wang, H. et al. Strong metal–support interactions on gold nanoparticle catalysts achieved through Le Chatelier’s principle. *Nat. Catal.* **4**, 418–424 (2021).
 - Montini, T., Melchionna, M., Monai, M. & Fornasiero, P. Fundamentals and catalytic applications of CeO₂-based materials. *Chem. Rev.* **116**, 5987–6041 (2016).
 - Zhai, Y. et al. Alkali-stabilized Pt-OH_x species catalyze low-temperature water–gas shift reactions. *Science* **329**, 1633–1636 (2010).
 - Yao, S. et al. Atomic-layered Au clusters on α-MoC as catalysts for the low-temperature water–gas shift reaction. *Science* **357**, 389–393 (2017).
 - Lee, Y.-L., Kim, K.-J., Hong, G.-R. & Roh, H.-S. Target-oriented water–gas shift reactions with customized reaction conditions and catalysts. *Chem. Eng. J.* **458**, <https://doi.org/10.1016/j.cej.2023.141422> (2023).
 - Li, L. et al. Multifunctional mesostructured silica microspheres from an ultrasonic aerosol spray. *Adv. Funct. Mater.* **18**, 2956–2962 (2008).
 - Zhu, Y. J. et al. Recent progress on spray pyrolysis for high performance electrode materials in lithium and sodium rechargeable batteries. *Adv. Ener. Mater.* **7**, 1601578 (2017).
 - Fu, X.-P. et al. Direct identification of active surface species for the water–gas shift reaction on a gold–ceria catalyst. *J. Am. Chem. Soc.* **141**, 4613–4623 (2019).
 - Yan, H. et al. Construction of stabilized bulk-nano interfaces for highly promoted inverse CeO₂/Cu catalyst. *Nat. Commun.* **10**, 3470 (2019).
 - Biesinger, M. C. et al. Resolving surface chemical states in XPS analysis of first row transition metals, oxides and hydroxides: Cr, Mn, Fe, Co and Ni. *Appl. Surf. Sci.* **257**, 2717–2730 (2011).
 - Tian, Y. et al. Engineering crystallinity and oxygen vacancies of Co(II) Oxide nanosheets for high performance and robust rechargeable Zn–Air batteries. *Adv. Funct. Mater.* **31**, 2101239 (2021).
 - Meng, Q., Liu, H., Xu, K., Wang, W. & Jia, C. CeO₂-x modified Ru/γ-Al₂O₃ catalysts for ammonia decomposition reaction. *Journal of Rare Earths*, <https://doi.org/10.1016/j.jre.2023.01.017> (2023).
 - Rivas-Murias, B. & Salgueiriño, V. Thermodynamic CoO-Co₃O₄ crossover using Raman spectroscopy in magnetic octahedron-shaped nanocrystals. *J. Raman Spectrosc.* **48**, 837–841 (2017).
 - Wu, Z., Li, M., Howe, J., Meyer, H. M. 3rd & Overbury, S. H. Probing defect sites on CeO₂ nanocrystals with well-defined surface planes by Raman spectroscopy and O₂ adsorption. *Langmuir* **26**, 16595–16606 (2010).
 - Ziembra, M. & Hess, C. Influence of gold on the reactivity behaviour of ceria nanorods in CO oxidation: combining operando spectroscopies and DFT calculations. *Catal. Sci. Tech.* **10**, 3720–3730 (2020).
 - Du, L. et al. Copper-ceria sheets catalysts: Effect of copper species on catalytic activity in CO oxidation reaction. *J. Rare Earths* **35**, 1186–1196 (2017).
 - Zhou, L., Wei, S., Wang, W., Jin, Z. & Jia, C. Au/La-CeO_x catalyst for CO oxidation: effect of different atmospheres pretreatment on gold state—Commemorating the 100th anniversary of the birth of Academician Guangxian Xu. *J. Rare Earths* **39**, 364–373 (2021).
 - Ahn, S.-Y. et al. Unravelling the active sites and structure-activity relationship on Cu–ZnO–Al₂O₃ based catalysts for water–gas shift reaction. *Appl. Catal. B: Environ.* **325**, 122320 (2023).
 - Lee, Y.-L. et al. Effect of alkali and alkaline earth metal on Co/CeO₂ catalyst for the water–gas shift reaction of waste derived synthesis gas. *Appl. Catal. A: Gen.* **551**, 63–70 (2018).
 - Parastaev, A. et al. Boosting CO₂ hydrogenation via size-dependent metal–support interactions in cobalt/ceria-based catalysts. *Nat. Catal.* **3**, 526–533 (2020).
 - Chen, W. et al. Molecular-Level Insights into the notorious CO poisoning of platinum catalyst. *Angew. Chem. Int. Ed.*, <https://doi.org/10.1002/anie.202200190> (2022).
 - Rodriguez, J. A. et al. Water–gas shift reaction on a highly active inverse CeO_x/Cu111 catalyst: unique role of ceria nanoparticles. *Angew. Chem. Int. Ed.* **48**, 8047–8050 (2009).
 - Jacobs, G. & Davis, B. H. Low temperature water–gas shift: applications of a modified SSITKA–DRIFTS method under conditions of H₂ co-feeding over metal/ceria and related oxides. *Appl. Catal. A: Gen.* **333**, 192–201 (2007).
 - Jha, A., Jeong, D.-W., Lee, Y.-L., Nah, I. W. & Roh, H.-S. Enhancing the catalytic performance of cobalt oxide by doping on ceria in the high temperature water–gas shift reaction. *RSC Adv.* **5**, 103023–103029 (2015).
 - Fu, X. P. et al. Facile fabrication of CeO₂-Al₂O₃ hollow sphere with atomically dispersed Fe via spray pyrolysis. *Inorg. Chem.* **60**, 5183–5189 (2021).

Acknowledgements

This work is funded by the National Key Research and Development Program of China (2021YFA1501103), the National Science Fund for Distinguished Young Scholars of China (22225110), the National Science Foundation of China (22075166, 22271177), the Young Scholars Program of Shandong University. We thank the Center of Structural Characterizations and Property Measurements at Shandong University for the help on sample characterizations.

Author contributions

C.-J.J. supervised the work; X.-P.F., C.-P.W. and C.-J.J. had the idea and designed the experiments. X.-P.F. and C.-J.J. analyzed the results and wrote the manuscript; X.-P.F. and C.-P.W. performed the catalytic tests, H₂-TPR and TPSR tests. X.-P.F. and W.-W.W. performed the in situ XRD, in situ Raman and quasi in situ XPS; X.-P.F., Z.J., and C.-P.W. designed and prepared the catalysts; J.-C.L. performed the DFT calculation; C.M. performed the aberration-corrected HAADF-STEM measurements and analyzed the results. All authors have given approval to the final version of the manuscript.

Competing interests

The authors declare no competing interest.

Additional information

Supplementary information The online version contains supplementary material available at <https://doi.org/10.1038/s41467-023-42577-9>.

Correspondence and requests for materials should be addressed to Jin-Cheng Liu, Chao Ma or Chun-Jiang Jia.

Peer review information *Nature Communications* thanks Hyun-Seog Roh, and the other, anonymous, reviewers for their contribution to the peer review of this work. A peer review file is available.

Reprints and permissions information is available at <http://www.nature.com/reprints>

Publisher's note Springer Nature remains neutral with regard to jurisdictional claims in published maps and institutional affiliations.

Open Access This article is licensed under a Creative Commons Attribution 4.0 International License, which permits use, sharing, adaptation, distribution and reproduction in any medium or format, as long as you give appropriate credit to the original author(s) and the source, provide a link to the Creative Commons licence, and indicate if changes were made. The images or other third party material in this article are included in the article's Creative Commons licence, unless indicated otherwise in a credit line to the material. If material is not included in the article's Creative Commons licence and your intended use is not permitted by statutory regulation or exceeds the permitted use, you will need to obtain permission directly from the copyright holder. To view a copy of this licence, visit <http://creativecommons.org/licenses/by/4.0/>.

© The Author(s) 2023